JGR Oceans

RESEARCH ARTICLE
10.1029/2024JC022034

# Influence of Transient Bottom Water Temperature Variations on Geothermal Heat Flow Measurements From the Bellingshausen Sea, West Antarctica, and the Baltic Sea

**Caroline Brand[1,2], Norbert Kaul[1], Mareen Lösing[3,4,5], and Karsten Gohl[6]**

[1]Faculty of Geosciences, University of Bremen, Bremen, Germany, [2]Now at Department of Geosciences, Aarhus University, Aarhus, Denmark, [3]School of Earth and Oceans, The University of Western Australia, Perth, WA, Australia, [4]Australian Centre for Excellence in Antarctic Science, The University of Western Australia, Perth, WA, Australia, [5]Institute of Geosciences, Kiel University, Kiel, Germany, [6]Alfred-Wegener-Institute Helmholtz-Centre for Polar and Marine Science, Bremerhaven, Germany

**Abstract** Geothermal heat flow (GHF) data provide important constraints for ice-sheet flow dynamics as GHF affects sliding conditions at the ice-bed contact and englacial temperatures. However, marine measurements of the geothermal gradients can get distorted down to ~3–10 m below seafloor by annual bottom water temperature variations. First-ever geothermal data from the Bellingshausen Sea shelf, West Antarctica, are presumably affected by temperature variations in the modified Circumpolar Deep Water (mCDW) over annual and multidecadal periods. As magnitude and resolution of temperature data are low in the Bellingshausen Sea, we test a 1D water-sediment model on Baltic Sea data, which includes long-term water temperature and semiannual GHF measurements. The model approximates the measured sub-bottom temperatures satisfactorily, although sparse data in Antarctica lead to uncertainties in reconstructed bottom water temperatures. Distortions in the geothermal gradients of the Bellingshausen Sea can be modeled using annual water temperature variations of ±0.03–0.15°C. However, the spatial heterogeneity of mCDW temperatures, recorded by heat flow lance sensors, shows no connection to geothermal gradient distortions. Therefore, the mCDW temperature variations are likely not strongly seasonal but are local changes of similar magnitude. Higher-resolution water temperature records are needed to quantify uncertainties through annual water temperature variations in the current measurement-derived GHF of 47–84 $mWm^{-2}$ in Ronne Entrance and 21–57 $mWm^{-2}$ in Eltanin Bay. Multidecadal ocean warming reduces the geothermal gradient by 16%–55% in the Bellingshausen Sea and leads to a reversed geothermal gradient in the Baltic Sea. This highlights the need to correct marine GHF for environmental factors.

**Plain Language Summary** Geothermal heat flow provides important constraints for ice-sheet flow dynamics as it affects the sliding conditions at the ice-bed contact and the temperature profile of the ice. However, subseafloor temperature gradients can be distorted down to 3–10 m below seafloor due to the annual variations in water temperature. First-ever geothermal data from the Bellingshausen Sea could be affected by temperature variations in the modified Circumpolar Deep Water (mCDW) over annual and multidecadal periods. A vertical 1-D model including water and sediment temperatures was tested on Baltic Sea data, as these contain a 66-year bottom water temperature time series and semiannual subseafloor temperatures. Model outcomes for the Bellingshausen Sea demonstrate that water temperature variations of ±0.03–0.15°C can explain the observed distorted geothermal gradients. Spatial analysis of the mCDW indicates that these water variations are likely local temperature variations and not a clearly defined seasonal water temperature signal. The model shows that uncertainties in measured geothermal gradients of the Bellingshausen Sea cannot be resolved due to low-resolution annual water temperature data, and thus, uncertainties remain in heat flow estimates of 21–84 $mWm^{-2}$. Additionally, bottom water warming recorded over the last decades further contributes to a reduction in the measured geothermal gradient.

**Key Points:**

- Marine geothermal heat flow (GHF) modeling shows the limit of reconstructing bottom water and sediment temperature variations in data-sparse areas
- First GHF measurements in the Bellingshausen Sea show temperature signals of local bottom water variations
- Climate change has reached the seafloor temperature gradients of the Baltic Sea and the Bellingshausen Sea (West Antarctica)

**Supporting Information:**

Supporting Information may be found in the online version of this article.

**Correspondence to:**

C. Brand,
carbrand@geo.au.dk

**Citation:**

Brand, C., Kaul, N., Lösing, M., & Gohl, K. (2025). Influence of transient bottom water temperature variations on geothermal heat flow measurements from the Bellingshausen Sea, West Antarctica, and the Baltic Sea. *Journal of Geophysical Research: Oceans*, *130*, e2024JC022034. https://doi.org/10.1029/2024JC022034

Received 25 OCT 2024
Accepted 10 JUL 2025

**Author Contributions:**

**Conceptualization:** Caroline Brand, Norbert Kaul
**Formal analysis:** Caroline Brand
**Funding acquisition:** Norbert Kaul, Karsten Gohl
**Investigation:** Caroline Brand, Norbert Kaul, Mareen Lösing
**Writing – original draft:** Caroline Brand
**Writing – review & editing:** Caroline Brand, Norbert Kaul, Mareen Lösing, Karsten Gohl



## 1. Introduction

Geothermal heat flow data provide insights into tectonic and magmatic developments, or contribute to ice-sheet models through the heat flow's influence on basal melt and ice rheology (e.g., Jordan et al., 2018; Larour et al., 2012; Reading et al., 2022). However, seasonal temperature variations in the bottom water can influence sub-bottom temperatures down to ~10 m below seafloor (Müller et al., 2016). Due to technical limitations, marine

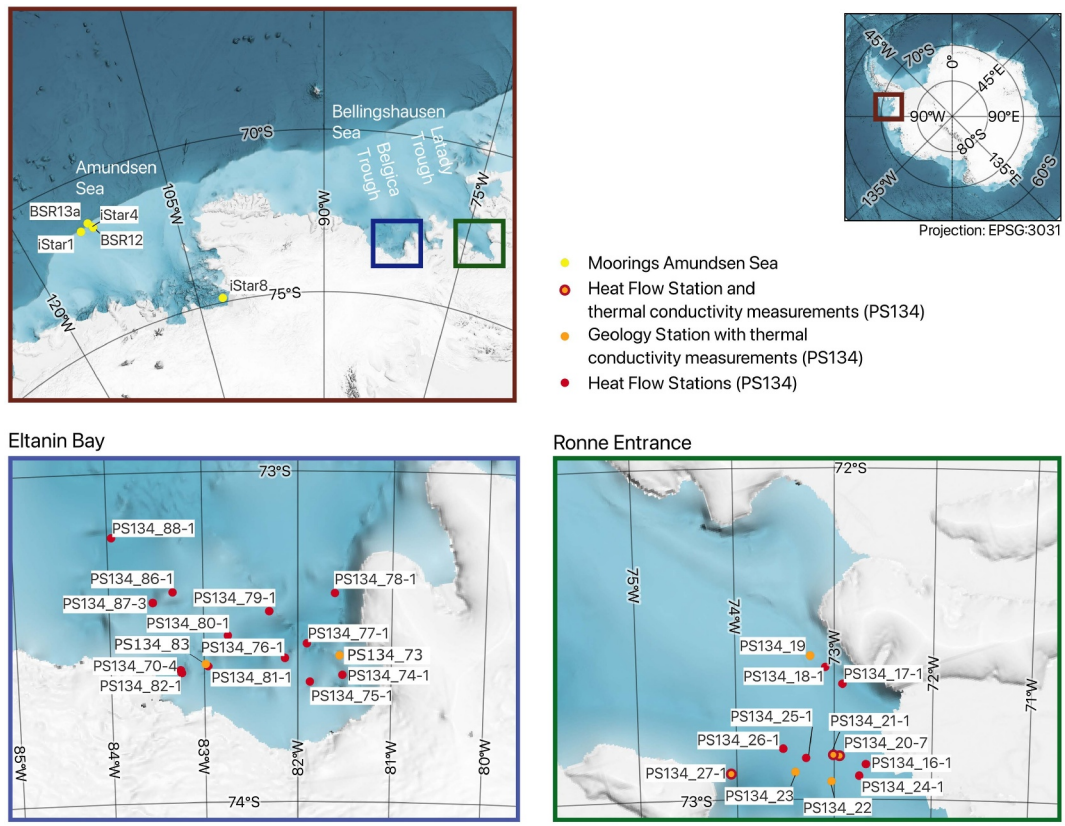


**Figure 1.** Mooring locations in the Amundsen Sea, heat flow stations, and locations of sediment cores with available thermal conductivity measurements from cruise PS134 in the Bellingshausen Sea. The map is based on the Quantarctica package (Matsuoka et al., 2021) and the IBCSO map (Dorschel et al., 2022).

heat flow lances are usually 5–6 m long. Therefore, the measured geothermal gradient represents the transient state rather than the linear, steady-state geothermal gradient, subsequently affecting the derived heat flow estimates. The Bellingshausen Sea of West Antarctica is an example in which a connection between bottom water variations and distorted geothermal gradients is suspected. Here, Circumpolar Deep Water (CDW) upwells from the depths of the continental rise and slope, mixes with the shelf water (then named modified CDW—mCDW), and intrudes into glacial troughs of the continental shelf as (near-)bottom water, causing subglacial melting of ice shelves (e.g., Smith et al., 1999; Talbot, 1988).

Within the Latady Trough on the eastern shelf leading from Ronne Entrance to the shelf break and the Belgica Trough on the central shelf from Eltanin Bay to the shelf break (Figure 1), a cyclonic current system could be detected (Zhang et al., 2016). This is represented by warmer mCDW in the eastern part of the troughs flowing onshore (Schulze Chretien et al., 2021). These temperatures are >1.4°C at 300–400 m depth in the eastern Latady Trough and >1.2°C in the eastern Belgica Trough. While circulating in the trough, the mCDW layer thickness reduces and cools (Schulze Chretien et al., 2021). Melting processes near the coast contribute to cooling to ∼1.1°C and freshening of the mCDW, which flows back to the shelf break on the western side of the troughs (Schulze Chretien et al., 2021). A perpetual difference in the mCDW temperatures between the eastern and western Bellingshausen Sea can be found with 0.22°C warmer waters in the eastern part (Schubert et al., 2021).

Adjacently, better-studied Amundsen Sea moorings revealed seasonal variations with a thinner and colder mCDW layer in austral spring and summer (October–December) near the shelf break and further on the shelf in Pine Island Bay (Assmann et al., 2013; Webber et al., 2017). Amplitudes of the mCDW temperature variations range between 0.3 and 1.0°C with the maximum amplitude at 500 m, decreasing with greater water depth (Webber et al., 2017). The signal of these bottom water variations can influence the upper 3 m of the sediment temperature measurements and has impacted GHF data (Dziadek et al., 2019).

In the current research, it is invested whether the mCDW in the Bellingshausen Sea can be a pendant to the Amundsen Sea. First information about the temporal evolution of the mCDW temperature changes and its spatial distribution on the Bellingshausen Sea shelf was gathered by seal-borne tags (Schubert et al., 2021; Zhang et al., 2016). However, the seal tag data show little evidence of seasonal variations. Only in the eastern Bellingshausen Sea, small mCDW temperature variations can be noticed with cooler water in summer (Schubert et al., 2021). Nevertheless, data sets with direct measurements for the Bellingshausen Sea still have significant spatial and temporal heterogeneities (compare Schubert et al., 2021). A modeling study by Oelerich et al. (2022) found evidence for irregular changes between cold and warm periods of the mCDW that occur in correlation with variations in the position and intensity of the Amundsen Sea low (ASL) pressure center as recorded in the Amundsen Sea (Jenkins et al., 2018; Thoma et al., 2008; Webber et al., 2017). Changes in wind and water regimes can cause temperature differences in the mCDW near the seafloor of 1.5–2°C in the Bellingshausen Sea (Oelerich et al., 2022).

Bottom water temperature changes over longer timescales have also been observed in the Bellinghausen Sea. Schmidtko et al. (2014) found a 0.01°C $yr^{-1}$ warming over the last 30 years of available records, which is expected to contribute to a reduction in the geothermal gradients.

To invert the imprinted signal of bottom water temperature fluctuations on a yearly and multidecadal time scale, a 1D heat transfer equation and a water-sediment temperature model according to Miesner et al. (2015) are implemented. Applying the model to the Bellingshausen Sea is challenging due to the magnitude and resolution of the temperature data. Therefore, the approach is first tested on data from the Baltic Sea, where numerous long-term water temperature records and high-resolution semiannual GHF measurements are available.

## 2. Data

### 2.1. Bellingshausen Sea

For the Bellingshausen Sea, in total, 22 heat flow stations were available of which 9 stations are located in Ronne Entrance and 13 in Eltanin Bay (Figure 1). The measurements were obtained in January and February 2023 during the RV Polarstern expedition PS134 (Gohl, 2023).

For the sediment temperature measurements, a 5 m long lance with a weight head was used. Five miniature temperature loggers were attached to the lance through fins, and one logger measuring the water temperature was attached to the weight head (Figure 2). After penetration of the seafloor, the lance was left for 8 min in the sediment until the frictional heat from the penetration dissipated. The MTLs recorded the temperature in an interval of 1 s. The resolution of the temperature loggers is 1 mK, and after calibration with high-precision thermometers, an absolute accuracy of several mK to 1 mK is reached (Dziadek et al., 2019; Pfender & Villinger, 2002). For calibration, the MTLs were mounted on a CTD rosette and lowered to 2000 m water depth (Gohl, 2023). The MTLs measurements were then corrected for their offset relative to the CTD readings. The time-temperature measurements by the heat flow lance were converted to stable sediment temperatures in depth using the HFred code, a heat flow reduction algorithm by Villinger and Davis (1987).

The steady-state geothermal gradient $g$ (or $\frac{\partial T}{\partial z}$) (°C $m^{-1}$) was determined by fitting a linear regression model to the measurements (Figure 2). The error of $g$ is given here as the standard error of prediction $\Delta$, where $g \pm \Delta$ corresponds to the 68% prediction interval and $g \pm 2\Delta$ to 95% prediction interval (The MathWorks Inc, 2023).

The thermal conductivities were measured on split sediment cores using the KD2 pro thermal properties analyzer with a 30-mm dual needle. The KD2 obtains the parameters with an accuracy of ±10% (Decagon Devices Inc, 2016). The measurements were corrected for the ambient laboratory temperature. This was done following

$$\lambda_{\text{sediment}(4°C)} = \frac{\lambda * \lambda^{\Phi}_{\text{water}(4°C)}}{\lambda^{\Phi}_{\text{water}(20°C)}}$$

with $\lambda^{\Phi}_{\text{water}(20°C)} = 0.6$ W $m^{-1}$ $K^{-1}$ (thermal conductivity of water at 20°C) (Ramires et al., 1995) and $\lambda^{\Phi}_{\text{water}(4°C)} = 0.57$ W $m^{-1}$ $K^{-1}$ (thermal conductivity of water at 4°C) assuming $\Phi = 60\%$ (porosity of the sediment) (Dziadek et al., 2019). For split sediment core PS134_73-2 and PS134_83-2, the $\lambda^{\Phi}_{\text{water}(20°C)}$ was changed to the

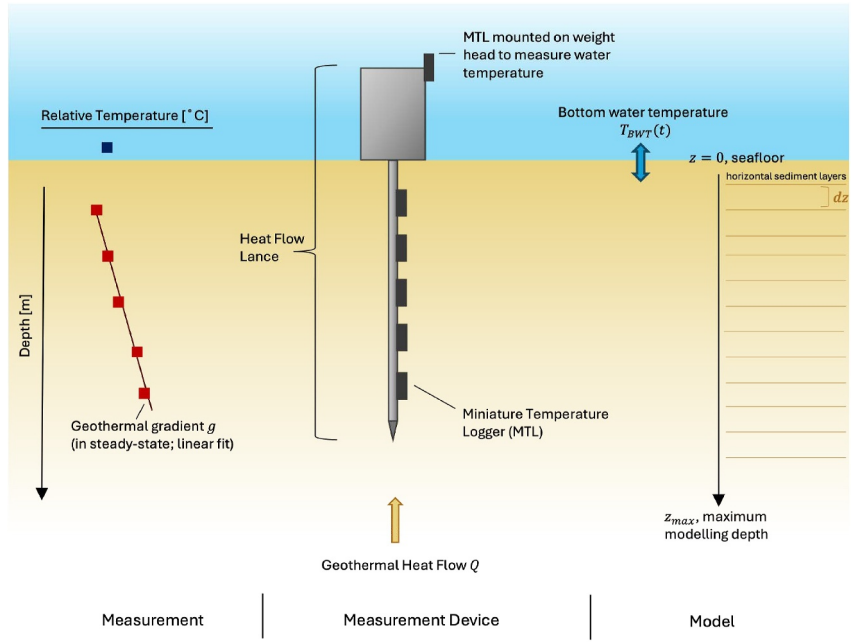


**Figure 2.** Schematic drawing of the measurement principle, the heat flow lance, and the water-sediment model after Miesner et al. (2015).

thermal conductivity of water at 7°C $\lambda^{\Phi}_{\text{water}(7^{\circ}\text{C})} = 0.5715$ W m$^{-1}$ K$^{-1}$ (Ramires et al., 1995), because the sediment cores stored at 4°C did not adjust to the laboratory temperature fully.

For the water-sediment model and the heat flow calculations, thermal conductivities were assigned to temperature measurements within a 10-km proximity with a similar geological setting. For all other temperature measurements, the mean thermal conductivity of each region was calculated. Using these conductivities and the geothermal gradient $g$, the heat flow $Q$ was estimated as follows:

$$Q = -\lambda\, g\ (\text{mW m}^{-2}).$$

The uncertainty of $Q$ is given by

$$\Delta Q = Q * \sqrt{\frac{\Delta g}{g^2} + \frac{\Delta \lambda}{\lambda^2}}$$

with $\Delta\lambda$ being the standard deviation.

For investigating the influence of possible bottom water variations, a selection of stations with deviations from the assumed linear temperature gradient and distortions with respect to the water temperature measurements were chosen (Figure 3). These include PS134_18, PS134_24, PS134_25, PS134_74, and PS134_86.

As no continuous long-term monitoring of the water masses in the Bellingshausen Sea exists, mooring data from the Amundsen Sea were used to gain a first idea of possible water temperature variations. The moorings recorded between 2009 and 2014 and were positioned at the shelf break and in Pine Island Bay at water depths between 513 and 1,465 m. For the purpose of our work, only the lowest sensors were used, which were mounted 24–31 m above the seafloor (Azaneu et al., 2023). The mooring program was supported by the iStar oceanographic program of the UK Natural Environment Research Council (iStar) (2018) and conducted during the Nathaniel B. Palmer expedition NBP0901 (BSR) (Huber & Jacobs, 2020).

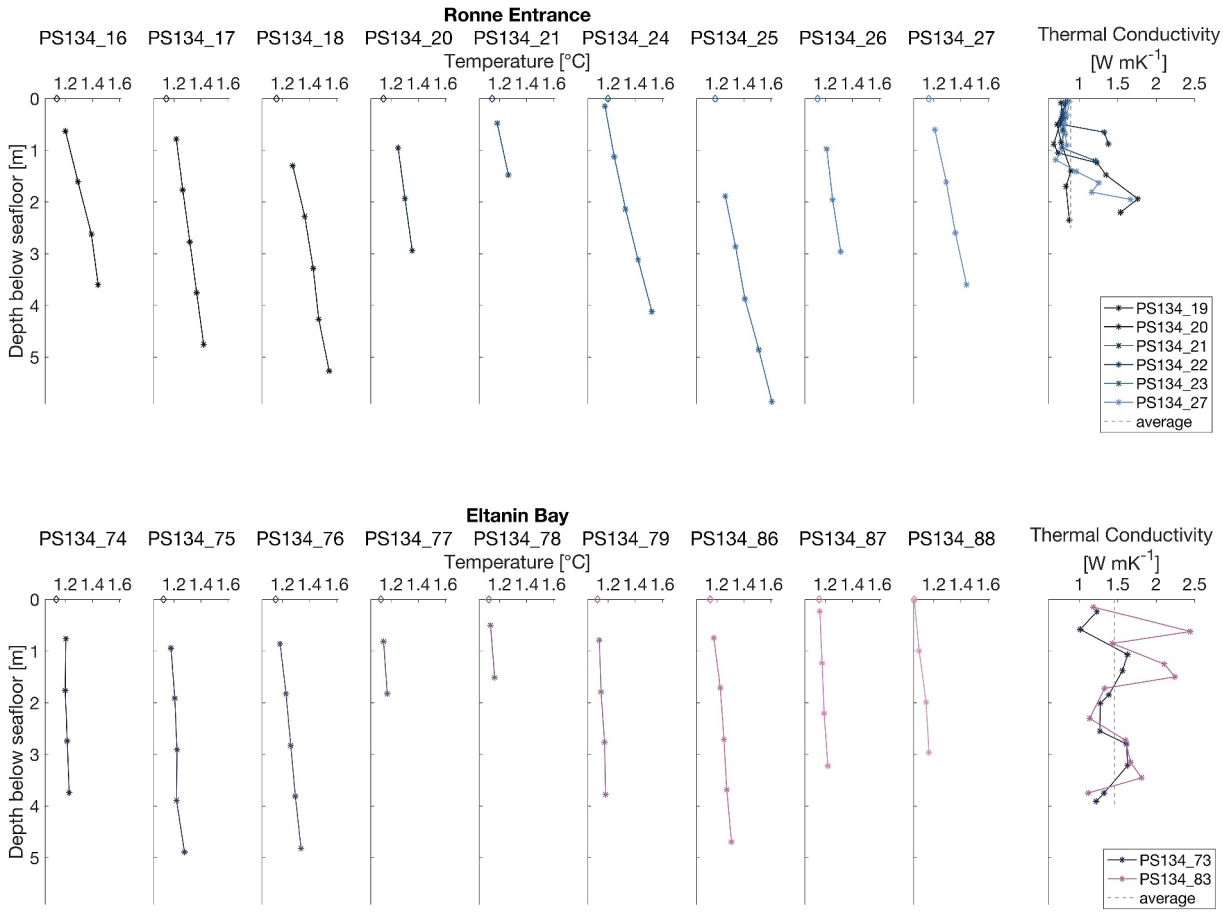


**Figure 3.** Measured sub-bottom temperatures (*), bottom water temperatures (⋄) (left), and measured thermal conductivities (right) of Ronne Entrance (top) and Eltanin Bay (bottom) in the Bellingshausen Sea.

### 2.2. Baltic Sea

Baltic Sea data were obtained during RV Alkor cruises AL584 and AL591 in Eckernförde Bay, revisiting the sites in November 2022 and April 2023 (Figure 4). During the two cruises, different lance types and measurement configurations were used (Table 1). At the two heat flow stations VH002/HF002, and VH006/HF006, temperature, thermal conductivity $\lambda$, thermal diffusivity $\kappa$, and heat capacity $c$ were determined. The temperature-time and conductivity measurements of cruise AL591 were converted to temperature-depth profiles and conductivity-depth profiles, respectively, with software by FIELAX based on an algorithm by Hartmann and Villinger (2002).

Long-term water temperature data were obtained from Boknis Eck (54.536°N, 10.040°E, water depth 28 m) for the period 30 April 1957–3 May 2022, with monthly measurements since 1957 (Bange & Malien, 2015; GEOMAR Helmholtz Centre for Ocean Research Kiel, 2023). Only measurements ≥25 m water depth were used to represent the bottom water.

## 3. Methods

### 3.1. Forward Model

To understand the water-sediment temperature interaction, we implemented a forward model that follows the work by Miesner et al. (2015) and Miesner (2018). The forward model uses a water temperature curve and a steady-state geothermal gradient, both approximated from data, to model the transient geothermal gradients, which represent geothermal gradients under the influence of bottom water temperature variability. For this model, some prerequisites were made. A 1D horizontally layered space was set to represent the seafloor ($z = 0$) and the

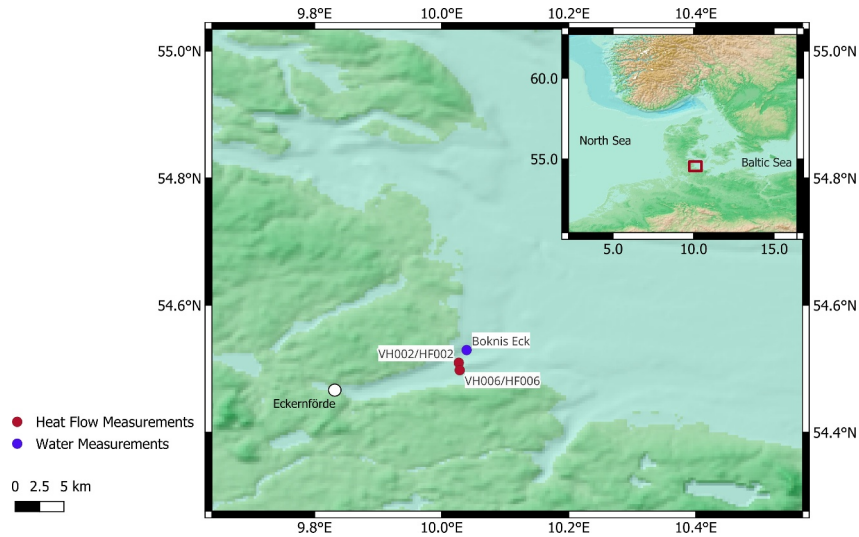


**Figure 4.** Selected heat flow stations of AL584 and AL591 and the location of water temperature measurements at Boknis Eck in the Eckernförde Bay, Baltic Sea. Bathymetry based on GEBCO (2023) grid.

sub-bottom sediment layers (Figure 2). The advection term of the heat transfer equation, heat sources, and other (lateral) fluid transports were neglected (Miesner et al., 2015). For modeling signals with the maximum time $t_{max} = 365$ days, a mesh size of $d_z = 0.025$ m and a time step $d_t = 0.05$ days were used. In premodeling tests by Miesner et al. (2015), these settings were proven to result in a model accuracy below the heat flow lance measurement accuracy (1 mK). The maximum modeling depth $z_{max}$ was set to 20 m to capture the penetration of a 1-year thermal signal, which is affecting the sediment temperature down to 8.7 m ($l = \sqrt{4\kappa t}$ (Irene, 2005) assuming $\kappa_{max} = 6*10^{-7}$ m$^2$ s$^{-1}$) (compare Miesner, 2018). For modeling temperature signals of a 30- and 66 year-period, $z_{max}$ was set to 100 m, as a maximum penetration depth $l$ of the thermal signal up to 70 m is expected. Due to computational capacities, the mesh size needed to be set to $dz = 0.25$ m.

**Table 1**
*Overview of Instruments and Methods Used During Cruise AL584 and AL591 for Measuring the Sub-Bottom Temperatures and Thermal Parameters λ, κ, c*

| | AL584—November | AL591—April |
|---|---|---|
| Position of station and water depth | VH002:<br>10.027000°E, 54.509540°N,<br>25.9 m<br>VH006:<br>10.028433°E, 54.497883°N,<br>25.7 m | HF002:<br>10.027006°E, 54.509608°N,<br>26.0 m<br>HF006:<br>10.028153°E, 54.497932°N,<br>26.8 m |
| Lance type (company) | Vibrocorer (MSH) with parallel mounted heat flow probe | Lance (GEOMAR) with outside mounted sensor string |
| Lance length | 3.75 m | 6 m |
| Channels (spacing) | 22 (15 cm) | 22 (25 cm) |
| Measurement time | 45 min | 40 min |
| Resolution sensors | 1 mK | 1 mK |
| Accuracy sensors | 2 mK | 2 mK |
| $\lambda, \kappa, c$ measurement tool (method) | KD2 Decagon Thermal Properties Analyzer (measurement every 15 cm on sediment core) | In situ (monitoring the decay of emitted heat pulse by heat flow probe) |
| Accuracy of $\lambda, \kappa, c$ measurements | ±5% to ±10% (Decagon Devices Inc, 2016) | 1%–3% (Hartmann & Villinger, 2002) |

The model by Miesner et al. (2015) consists of two main equations, the heat transfer equation and the bottom water temperature time series. The water temperature equation is described by a cosine function, representing a symmetrical temperature profile with a seasonal minima and a maxima as follows:

$$T_{\mathrm{BWT}}(t) = A + B * \cos(\omega t + \varphi)$$

To approximate nonsinusoidal water temperature variations, $T_{\mathrm{BWT}}(t)$ was expressed as a Fourier series (compare Miesner et al., 2015) as follows:

$$T_{\mathrm{BWT}}(t) = A + \sum_{i=1}^{n} B_n * \cos\left(n * \omega * t + \varphi_n\right)$$

with $T_{\mathrm{BWT}}(t)$ = water temperature (°C), $A$ = average temperature (°C), $B$ = amplitude (°C), $\omega$ = period of $\frac{2\pi}{365}$, and $\varphi$ = phase delay with $\varphi = \omega(d)$, where $d$ = day of annual temperature minimum. When using the forward model (without inversion), the parameters of $T_{\mathrm{BWT}}$ were approximated from the measurements by minimizing the sum of squared error between $T_{\mathrm{BWT}}$ and the water temperature time series using the Nelder-Mead simplex algorithm implemented in the fminsearch Matlab solver (Lagarias et al., 1998; The MathWorks Inc, 2023).

To incorporate the effect of constant ocean warming on the temperature gradients, the forward model was run to simulate 66 years for the Baltic Sea, which covers the time span of the Boknis Eck water temperature time series. From this time series, a linear trend in bottom water warming $\Delta A_{\mathrm{decadal}}$ (°C $\mathrm{s}^{-1}$) was calculated and added to $T_{\mathrm{BWT}}(t)$. In the Bellingshausen Sea, $\Delta A_{\mathrm{decadal}}$ is represented by a warming of 0.01°C $\mathrm{yr}^{-1}$ over 30 years of available observations from Schmidtko et al. (2014). As determining annual water temperature variations is more challenging in this area, the seasonal temperature components $B$ and $\varphi$ have been set to zero to focus solely on the multidecadal water temperature variations.

The sediment temperature is described as a sum of the temperature field $u$ and the geothermal gradient $g$ as follows:

$$T_{\mathrm{total}}(z,t) = u(z,t) + gz$$

Usually, the geothermal gradient can be determined from the measurements itself, except for the Baltic Sea, where due to a massive measurement distortion, the literature value of 0.03°C $\mathrm{m}^{-1}$ is used for the forward model (Fuchs et al., 2023).

The temperature field $u$ consists of the heat transfer equation as follows:

$$\partial_t u(z,t) - \partial_z\left(\kappa(z)\partial_z u(z,t)\right) = 0$$

with $\kappa$ = thermal diffusivity ($\mathrm{m}^2\ \mathrm{s}^{-1}$). Thermal diffusivities were determined in situ or on split cores for the Baltic Sea. In the case of the Bellingshausen Sea, $\kappa$ was calculated using a volumetric heat capacity of 3,400,000 J $\mathrm{K}^{-1}$ $\mathrm{m}^{-3}$, typical for water-saturated clay/silt (Andujar Marquez et al., 2016), and the following relation of $\kappa = \frac{\lambda}{\rho c}\left(\mathrm{m}^2\mathrm{s}^{-1}\right)$. The resulting thermal diffusivities were interpolated to fit the model mesh and implemented as a piecewise constant function.

As the numeric model requires an initial sediment temperature field for $t = 0$, the analytical solution after Carslaw and Jaeger (1939) is used as follows:

$$T(z,t) = A + g * z + B * \exp\left(-\sqrt{\frac{\omega}{(2\kappa)}}z\right) * \cos\left(\omega t - \sqrt{\frac{\omega}{2\kappa}}z + \varphi\right)$$

The upper boundary of the model, $z = 0$ m (seafloor), is described by the water temperature equation and its interaction with the sediment temperature as follows:

$$\kappa(z)\partial_z u(0,t) = \frac{h}{\rho c_v}(u(0,t) - T_{\text{water}}(t))$$

with $h$ = the heat transfer coefficient (W m$^{-2}$ K$^{-1}$), $\rho c_v$ = volumetric heat capacity (J K$^{-1}$ m$^{-3}$). The heat transfer coefficient is set to $h$ = 150 W m$^{-2}$ K$^{-1}$ for all simulations, following the setup by Miesner et al. (2015). This value is typical for the Baltic Sea, and variations of the parameter have little influence (Brakelmann & Stammen, 2006; Miesner et al., 2015). For $\rho c_v$, we use 3,692,618 J K$^{-1}$ m$^{-3}$ for station VH002/HF002 and 3,602,319 J K$^{-1}$ m$^{-3}$ for station VH006/HF006 in the Baltic Sea, and 3,400,000 J K$^{-1}$ m$^{-3}$ for the Bellingshausen. The water-sediment boundary is a Robin boundary condition that allows heat to flow toward the cooler space (Miesner et al., 2015).

At the lower boundary, only the (linear) background geothermal gradient with respect to the average water temperature prevails as follows:

$$\partial_z u(z_{\max}, t) = A + g * z_{\max}$$

This is implemented using a Neumann boundary condition.

The partial differential equations of the model are solved by the pdepe solver of Matlab (Skeel & Berzins, 1990; The MathWorks Inc, 2023). The time integration is performed by the ode15s solver (Shampine & Reichelt, 1997; The MathWorks Inc, 2023).

### 3.2. Inverse Model

The measured transient geothermal gradients were inverted to reconstruct the bottom water temperature and the steady-state geothermal gradient. For this, we used the delayed rejection adaptive Metropolis algorithm (DRAM) developed by Haario et al. (2006), which was already tested for the water-sediment model by Miesner (2018). The DRAM algorithm uses the Markov Chain Monte Carlo (MCMC) method and combines a delayed rejection with an adaptive MCMC. First, a candidate, $y_1$, is drawn from a Gaussian proposal distribution with a covariance matrix. The initial covariance matrix $C_0$ is set based on available data information from, for example, measurements (Haario et al., 2006).

The adaptive Metropolis component of the DRAM updates the covariance matrix as the MCMC chain progresses, with the proposal distribution centered around the current chain position (Haario et al., 2006). The covariance matrix $C_n$ is defined as follows:

$$C_n = \begin{cases} C_0, & n \le n_0 \\ s_d Cov(X_0, \ldots, X_{n-1}) + s_d \varepsilon I_d, & n > n_0 \end{cases}$$

with $n_0$ = the time index of the initial nonadaptation period, $s_d$ is a parameter dependent on the dimension of the state space on which the distribution is chosen, and $I_d$ d-dimensional identity matrix; parameter $\varepsilon$ ensures that the covariance matrix is not singular (Haario et al., 2006). For the proposal of a new state, $C_n^i$ is a scaled version of the first stage $C_n^1$ (Haario et al., 2006):

$$C_n^i = \gamma_i C_n^1$$

In the principal of the delayed rejection, the first-stage candidate, $y_1$, is accepted with probability $\alpha_1$:

$$\alpha_1(x, y_1) = \min\left(1, \frac{\pi(y_1)\, q_1(y_1, x)}{\pi(x)\, q_1(x, y_1)}\right)$$

where $q_1(x, \cdot)$ = first-stage proposal distribution and $\pi$ = distribution of current candidate (Haario et al., 2006).

If the first-stage candidate is rejected, a new second-stage proposal relies on the current chain position and rejected proposal distribution (Haario et al., 2006). The proposal of the second stage is then accepted with the probability $\alpha_2$ as follows:

$$\alpha_2(x,y_1,y_2) = \min\left(1, \frac{\pi(y_2)\, q_1(y_2,y_1)\, q_2(y_2,y_1,x)\left[1-\alpha_1(y_2,y_1)\right]}{\pi(x)\, q_1(x,y_1)\, q_2(x,y_1,y_2)\left[1-\alpha_1(x,y_1)\right]}\right)$$

with $y_2$ = second-stage candidate, and $q_2(x,y_1,\cdot)$ = second-stage proposal (Haario et al., 2006).

This delayed rejection can be iterated for multiple stages of proposals (Haario et al., 2006). The combination of delayed rejection and adaptive Metropolis increases the efficiency of the DRAM compared to other MCMC/AM algorithms if no good initial proposal distribution can be given (Haario et al., 2006). The DRAM algorithm was implemented in the water-sediment model by adapting the DRAM code for Matlab and MCMC toolbox by Laine (2011, 2018).

## 4. Results

### 4.1. Model Test on Baltic Sea Data

The water temperature time series from Boknis Eck reveals large interannual deviations with differences in the mean annual water temperature of ∼1.7°C, temperature amplitude of ∼1.4°C, and a variance of the day of minimum temperature of 14 days for the years 2020–2021. The simple cosine water temperature function, as used by most studies (e.g., Miesner et al., 2015; Neumann et al., 2017), shows relative errors between the approximated curve and the water temperature measurements of >16% ($T_{\mathrm{BWT}}(t)$, $n = 1$). The best fit is obtained by fitting a summation of cosines with three different periods to the average water temperature time series of 2019–2021 (relative error of 8.57%; $A = 8.35$°C, $B_1 = 4.04$°C, $B_2 = 0.53$°C, $B_3 = 0.12$°C, and $\varphi = 1.74$) (Figure 5a). The single measurement time series of 2021 could not be approximated with a relative error better than 37% (Figure S1 and Table S1 in Supporting Information S1).

The parameter values from the best curve approximation (mean temperature 2019–2021, $n = 3$) were used as input for the forward water-sediment-temperature model. For station VH006/HF006, this results in a maximum relative error between the sub-bottom temperature measurements and the modeled solution on the day of measurement of 10.52% (AL584, November) and 7.69% (AL591, April) (Figure 5a). The relative error decreases to 8.07% (AL584, November) and 4.94% (AL591, April) when changing the mean annual temperature to 8.6°C.

The inversion tested on station VH006/HF006 shows high standard deviations for the reconstructed amplitudes $B_1, B_2, B_3$, and the geothermal gradient (Table 2). The amplitudes do not fully represent the water temperature measurements (Figure 5b) and their mean estimates deviate by 30%–100% from $T_{\mathrm{BWT}}$ that has been approximated to the Boknis Eck measurements using fminsearch. The mean annual temperature $A$ shows a lower standard deviation that is below 4% of the mean estimate (Table 2) and deviates from the average water temperature measurements from 2019 to 21 by only 1% (Table 2). Overall, the inversion yields a relative error between measurement and modeled sub-bottom temperature on the day of measurement below 10%. The lowest water temperatures are in January/February, which is consistent with the measurements of the Boknis Eck time series.

### 4.2. Heat Flow Lance Recordings in the Bellingshausen Sea

The temperature and thermal conductivity measurements exhibit differences between Ronne Entrance and Eltanin Bay, which result in a generally lower GHF in Eltanin Bay than in Ronne Entrance (Table 3).

The mCDW (>1.0°C) recorded by the heat flow lance has a temperature maximum of 1.20°C in Eltanin Bay and 1.30°C in Ronne Entrance at around 550 m in both locations (Figure 6). Deviating from that are stations PS134_86, PS134_87, and PS134_88 in the western Eltanin Bay, which show a shallower onset of the mCDW. In Ronne Entrance, the northeasternmost station PS134_18 indicates a deeper mCDW onset.

The mCDW temperature decreases to 1.06–1.16°C close to the seafloor in Eltanin Bay, whereas in Ronne Entrance, water temperatures decrease to 1.14–1.18°C (Figure 6). The coldest bottom water temperature in Eltanin Bay can be found at the deepest station PS134_88. The deepest measurement of Ronne Entrance on the other hand shows a slightly warmer mCDW of 1.16°C than other measurements in the area.

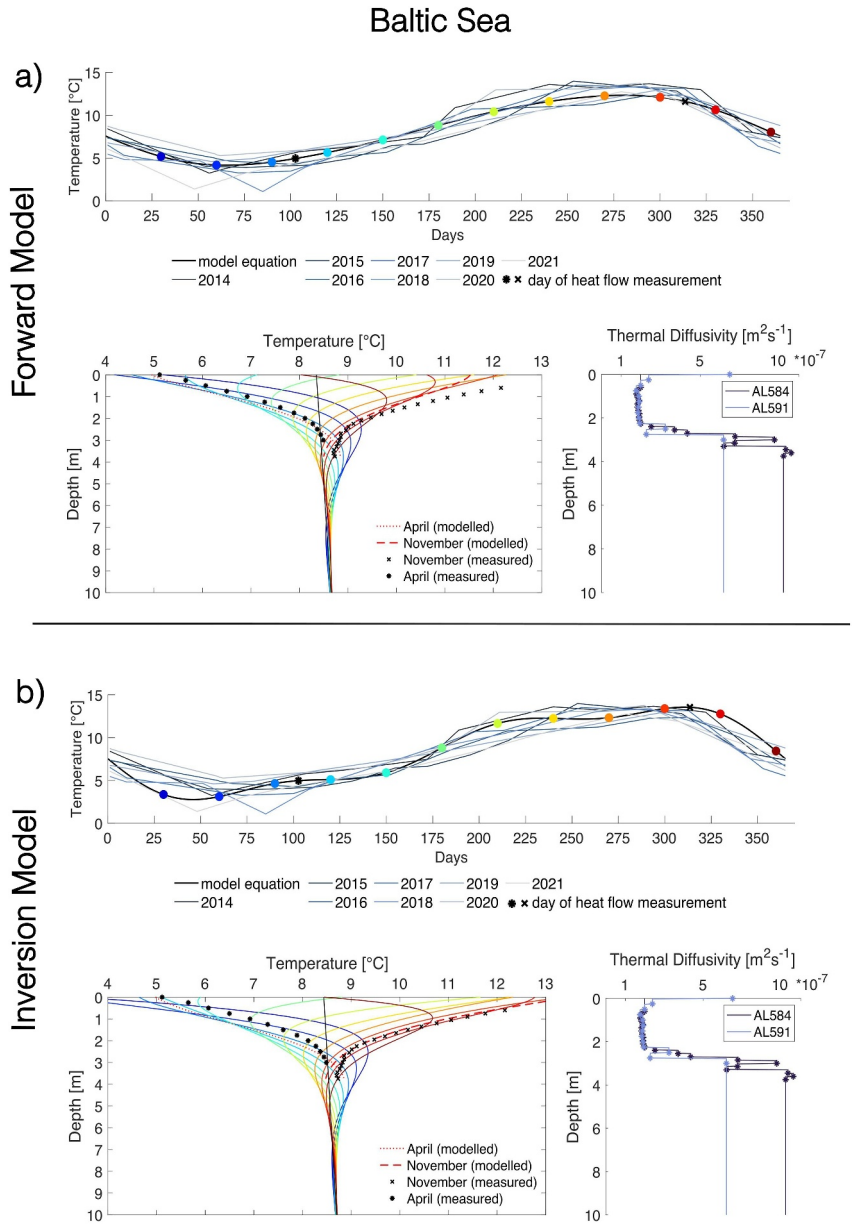


**Figure 5.** The forward model (a) and the inversion model (b) for the station VH006/HF006, Baltic Sea. Top panel of (a): $T_{\mathrm{BWT}}(t)$ with parameters approximated from measurements of 2019–2021. Top panel of (b): $T_{\mathrm{BWT}}(t)$ with parameters obtained by the DRAM inversion. Bottom left of (a and b): Modeled geothermal gradients. The colors represent a transient geothermal gradient at a certain time of the water temperature time series. Bottom right of (a, and b): The measured (*) and model-interpolated (−) thermal diffusivities. Both models only consider the thermal diffusivities of cruise AL584.

### 4.3. Forward Modeling of the Bellingshausen Sea Data

Fitting $T_{\mathrm{BWT}}$ to the moorings in the adjacent Amundsen Sea yields a phase delay with a variable value ($\varphi = 2.4$, 2.9, 3.9, 4.7), resulting in minimum temperatures between October and February, depending on the mooring station and year. The amplitudes of the water temperature variations are relatively low at ±0.03°C and ±0.05°C. The simplex search method of the fminsearch solver smoothed a lot of outliers and does not approximate high temperature events (Table S2 and Figure S2 in Supporting Information S1).

**Table 2**
*Results of the Forward Model and Its Inversion (Run With 50,000 Chain Members) for the Baltic Sea and the Bellingshausen Sea*

| | Station | $A$ (°C) | $B_1$ (°C) | $B_2$ (°C) | $B_3$ (°C) | $\varphi$ (d) | $g$ (°C m$^{-1}$) | Max. rel. error |
|---|---|---|---|---|---|---|---|---|
| Baltic Sea | | | | | | | | |
| Forward | VH006/HF006 | 8.35 | 4.04 | 0.53 | 0.12 | 1.74 | – | 10.52% (AL584), 7.69% (AL591) |
| Inversion | VH006/HF006 | 8.438 (0.311) | 5.081 (1.521) | 0.937 (1.847) | 1.816 (2.460) | 1.697 (0.263) | 0.026 (0.049) | 3.06% (AL584), 9.17% (AL591) |
| Bellingshausen Sea | | | | | | | | |
| Forward[a] | | | | | Ronne Entrance | | | |
| | PS134_18 | 1.200 | 0.030 | – | – | 4.700 | – | 1.72% |
| | PS134_24 | 1.160 | 0.050 | – | – | 4.700 | – | 0.83% |
| | PS134_25 | 1.095 | 0.050 | – | – | 4.700 | – | 1.22% |
| | | | | | Eltanin Bay | | | |
| | PS134_74 | 1.175 | 0.050 | – | – | 4.700 | – | 0.67% |
| | PS134_86 | 1.180 | 0.050 | – | – | 3.900 | – | 1.24% |
| Inversion | | | | | Ronne Entrance | | | |
| | PS134_18 | 1.225 (0.041) | 0.081 (0.071) | – | – | 2.556 (1.531) | 0.059 (0.010) | 0.91% |
| | PS134_24 | 1.126 (0.028) | 0.061 (0.020) | – | – | 5.356 (0.631) | 0.097 (0.008) | 0.83% |
| | PS134_25 | 1.102 (0.042) | 0.046 (0.070) | – | – | 1.997 (2.597) | 0.084 (0.010) | 1.51% |
| | | | | | Eltanin Bay | | | |
| | PS134_74 | 1.182 (0.050) | 0.041 (0.068) | – | – | 2.821 (2.124) | 0.014 (0.013) | 3.08% |
| | PS134_86 | 1.174 (0.053) | 0.058 (0.070) | – | – | 2.008 (2.167) | 0.027 (0.013) | 1.69% |

*Note.* The inversion result of each parameter is given as the mean (standard deviation). [a]Parameters are the approximations to the Amundsen Sea mooring time series that lead to the lowest relative error fitting the geothermal gradients.

To represent the temperature records from the moorings in the Amundsen Sea, amplitudes of ±0.03, ±0.05, and ±0.15°C (based on 0.3°C from Webber et al. (2017)) with phase shifts of 3.9 and 4.7 were tested as input for the forward model. Because annual water temperatures in the Bellingshausen Sea are expected to be warmer than in the Amundsen Sea between 2009 and 2014, the mean annual temperature is fitted to match the data (Table 2). For station PS134_86, the best fit is obtained using $\varphi = 3.9$ with a day of temperature minimum in December, whereas for all other stations, $\varphi = 4.7$ with a temperature minimum in October yields a closer fit (Table 2, Figure 7). Solutions with amplitudes of ±0.03 and ±0.05°C give similar results. The relative model error increases up to 6.4% for all stations when using a larger amplitude of ±0.15°C (Table S4 in Supporting Information S1).

As in situ thermal properties could not be measured for each station, further sensitivity tests were made to test the influence of using average thermal conductivities and resulting diffusivities for the Bellingshausen Sea data (Text S2, Figures S7 and S8 in Supporting Information S1). The estimation of $\kappa$ has only a small, negligible effect on the model accuracy (<0.74%).

### 4.4. Inversion of the Bellingshausen Sea Data

The mean parameter estimates from the inversion obtain a model solution that is in accordance with the measurements as the relative errors stay below 4% (Table 2). The mean annual temperatures have overall values of 1.10–1.23°C (Table 2). Their standard deviations remain low and are less than 4.5% of the mean estimate. The reconstructed water temperature amplitudes are between ±0.04–0.08°C with large standard deviations above 100% from the mean estimation (Table 2). The phase shifts of the possible water temperature variations show rather large standard deviations, which are up to >100% of the mean estimated value (Table 2). Except for PS134_24, the phase shifts lead to a temperature minimum from January to March (Figure 8, Figure S3–S6, Table S5 in Supporting Information S1). Nevertheless, the inversion statistics indicate that the inversion did not converge and did not reach a stable solution. Consequently, the results are subject to greater uncertainty.

The reconstructed geothermal gradients differ by 2%–10% from the measured geothermal gradients. Subsequently, heat flow values differ by 1–8 mWm$^{-2}$ (compare Tables 2 to Table 3). The reconstructed bottom water

**Table 3**
*The Geothermal Heat Flow for All Stations in the Bellingshausen Sea as Determined From Measurements During Expedition PS134*

| | Station | Longitude (°W) | Latitude (°S) | Water depth (m) | $g$ (°C m$^{-1}$) | $\pm\Delta g$ (°C m$^{-1}$) | $\lambda$ (W m$^{-1}$ K$^{-1}$) | $\pm\Delta\lambda$ (W m$^{-1}$ K$^{-1}$) | $Q$ (mW m$^{-2}$) | $\pm\Delta Q$ (mW m$^{-2}$) |
|---|---|---|---|---|---|---|---|---|---|---|
| Ronne Entrance | PS134_16 | −72.6754 | −72.8940 | 680 | 0.083 | 0.021 | 0.929[a] | 0.283 | 77 | 2 |
| | PS134_17 | −72.9171 | −72.6516 | 768 | 0.051 | 0.001 | 0.929[a] | 0.283 | 47 | 1 |
| | PS134_18 | −73.0912 | −72.6005 | 657 | 0.065 | 0.017 | 0.821 (PS134_19)[b] | 0.068 | 53 | 2 |
| | PS134_20 | −72.9467 | −72.8686 | 674 | 0.052 | 0.001 | 1.066 (PS134_20)[b] | 0.411 | 55 | 1 |
| | PS134_21 | −73.0086 | −72.8659 | 667 | 0.083 | –[c] | 1.014 (PS134_21)[b] | 0.311 | 84 | – |
| | PS134_24 | −72.7431 | −72.9289 | 723 | 0.088 | 0.014 | 0.929[a] | 0.283 | 82 | 1 |
| | PS134_25 | −73.2874 | −72.8754 | 752 | 0.086 | 0.015 | 0.929[a] | 0.283 | 80 | 2 |
| | PS134_26 | −73.5224 | −72.8468 | 761 | 0.052 | 0.008 | 0.929[a] | 0.283 | 48 | 2 |
| | PS134_27 | −74.0578 | −72.9214 | 1,099 | 0.077 | 0.006 | 0.923 (PS134_27)[b] | 0.284 | 71 | 1 |
| Eltanin Bay | PS134_70 | −83.2532 | −73.5988 | 798 | –[d] | – | – | – | – | |
| | PS134_74 | −81.5220 | −73.6160 | 605 | 0.015 | 0.001 | 1.378 (PS134_73)[b] | 0.205 | 21 | 2 |
| | PS134_75 | −81.8706 | −73.6371 | 752 | 0.022 | 0.019 | 1.511[e] | 0.374 | 33 | 6 |
| | PS134_76 | −82.1374 | −73.5651 | 920 | 0.038 | 0.004 | 1.511[e] | 0.374 | 57 | 2 |
| | PS134_77 | −81.9038 | −73.5210 | 1,016 | 0.027 | –[c] | 1.511[e] | 0.374 | 41 | – |
| | PS134_78 | −81.6082 | −73.3688 | 931 | 0.030 | –[c] | 1.511[e] | 0.374 | 45 | – |
| | PS134_79 | −82.3029 | −73.4236 | 695 | 0.017 | 0.007 | 1.511[e] | 0.374 | 26 | 5 |
| | PS134_80 | −82.7445 | −73.4961 | 559 | –[d] | – | – | – | – | – |
| | PS134_81 | −82.9588 | −73.5881 | 852 | –[d] | – | 1.643 (PS134_83)[b] | 0.462 | – | – |
| | PS134_82 | −83.2425 | −73.6076 | 824 | –[d] | – | – | – | – | – |
| | PS134_86 | −83.3226 | −73.3632 | 711 | 0.028 | 0.007 | 1.511[e] | 0.374 | 42 | 3 |
| | PS134_87 | −83.5347 | −73.3935 | 639 | 0.020 | 0.005 | 1.511[e] | 0.374 | 30 | 4 |
| | PS134_88 | −83.9528 | −73.1944 | 1,148 | 0.038 | 0.010 | 1.511[e] | 0.374 | 57 | 3 |

[a]Average thermal conductivity from split sediment cores measured in Ronne Entrance. [b]Station number of split sediment cores where thermal conductivities were measured. [c]Standard deviation could not be determined because only two loggers penetrated the seafloor. [d]Heat flow lance presumably tipped/not penetrated subsurface. [e]Average thermal conductivity from split sediment cores measured in Eltanin Bay.

variations can theoretically cause deviations of 64% in the geothermal gradient within the upper 5 m below seafloor over the course of a year (Table 4).

### 4.5. Multidecadal Ocean Warming

In addition to annual bottom water variations, multidecadal water temperature increases can be determined. The Boknis Eck measurements in the Baltic Sea show an increase of 0.0285°C yr$^{-1}$ from 1957 to 2022 (compare Figures 5 and 9, upper panels; Figure S1 in Supporting Information S1). For running the water-sediment model, $A = 6.53$°C was set as determined from the initial measurement period of 30 April 1957–10 April 1958. With this bottom water warming over 66 years, the geothermal gradient changes from 0.03 to −0.063°C m$^{-1}$, showing a reversal of the gradient in the upper 5 m of the sediment and the same negative trend as the temperature measurements of station VH002/HF002 (Figure 9). For this station, the maximum relative error between the model solution on the measurement day and the measurement itself is 7.49% for November (AL584) and 11.76% for April (AL591). The thermal signal $l$ of the constant water warming extends down to 41 m in the sediment (assuming $\kappa = 2 * 10^{-7}$ m$^{-2}$s$^{-1}$).

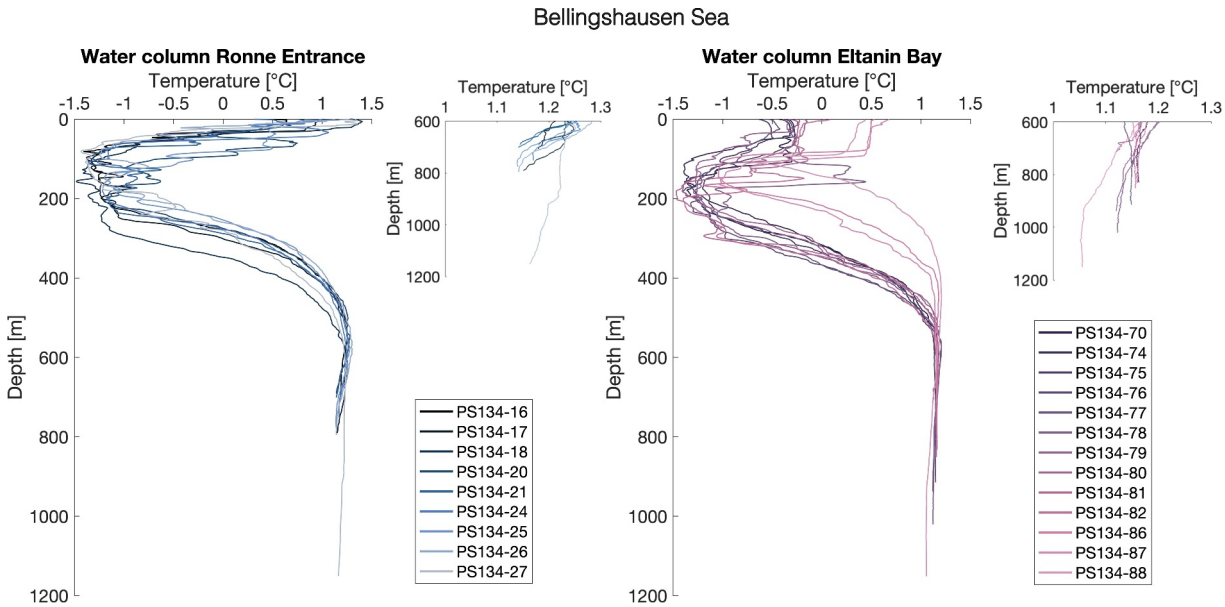


**Figure 6.** Water column temperatures measured by the heat flow lance during deployment in Ronne Entrance (left) and Eltanin Bay (right) in January/February 2023. With the winch speed, the water depth could be reconstructed from the heat flow logger recording time with an uncertainty of ∼50 m. Colormaps by Crameri (2018).

The multidecadal bottom water warming has also been observed in the Bellingshausen Sea with an increase of 0.01°C $yr^{-1}$ over 30 years (Schmidtko et al., 2014). In Ronne Entrance, the constant warming in bottom water temperature leads to a 20%–37% change in the measured geothermal gradients and, in Eltanin Bay, to a 39%–127% reduction in geothermal gradients (Table 4, Figure 10). The heat flow values, after correction of the constant water warming, are 16–26 $mWm^{-2}$ lower than heat flow values obtained from the measurements.

## 5. Discussion

### 5.1. Model Accuracy

The forward and inverse models of the Baltic Sea result in modeled geothermal gradients with a 9% relative error to the sub-bottom temperatures. In fact, the high accuracy of the heat flow measurements, 2 mK for sub-bottom temperatures and, for example, 0.5% for thermal parameters from cruise AL591, would allow an approximation of the sub-bottom temperature measurements with a lower model error. However, sensitivity tests by Miesner et al. (2015) showed that adding 8% noise to the water temperature increases the mean reconstruction error by 5%. Considering the interannual variability, noise in the Baltic Sea temperature, and the residual misfit of the approximated water temperature curve to the Boknis Eck measurement, the model solution can sufficiently replicate the temperature-depth profiles.

The Baltic Sea model tests demonstrate that input parameters derived from water measurements can achieve close fits of modeled transient sub-bottom geothermal gradients. Therefore, using Amundsen Sea mooring data as the $T_{BWT}(t)$ input for the forward model can be a good tool to demonstrate how mCDW variations in the Bellingshausen Sea would affect the heat flow measurements. Nevertheless, the mooring data in the Amundsen Sea, as such data from the Bellingshausen Sea shelf, reveal a noisy mCDW temperature signal (Figure 8, top), affected by interannual variations in the onset of the cooling phase, tidal currents, and currents induced by local atmospheric pressure variations (Assmann et al., 2013; Schulze Chretien et al., 2021; Webber et al., 2017). Additionally, $T_{BWT}(t)$ is described as a simple cosine as the Baltic Sea inversion shows that more complex water equations are challenging to reconstruct, especially when considering the unknown long-term behavior of the Bellingshausen Sea waters. The consideration of both aspects introduces some inaccuracies to the model. The forward model, using mooring data from the Amundsen Sea, sufficiently approximates the measured sub-bottom temperatures (Table 2, Table S4 in Supporting Information S1). However, the approach describing water temperature variations by a cosine causes high standard deviations in the inversion results for the Bellingshausen Sea, as sensitivity tests show (Text S1, Tables S6 and S7 in Supporting Information S1).

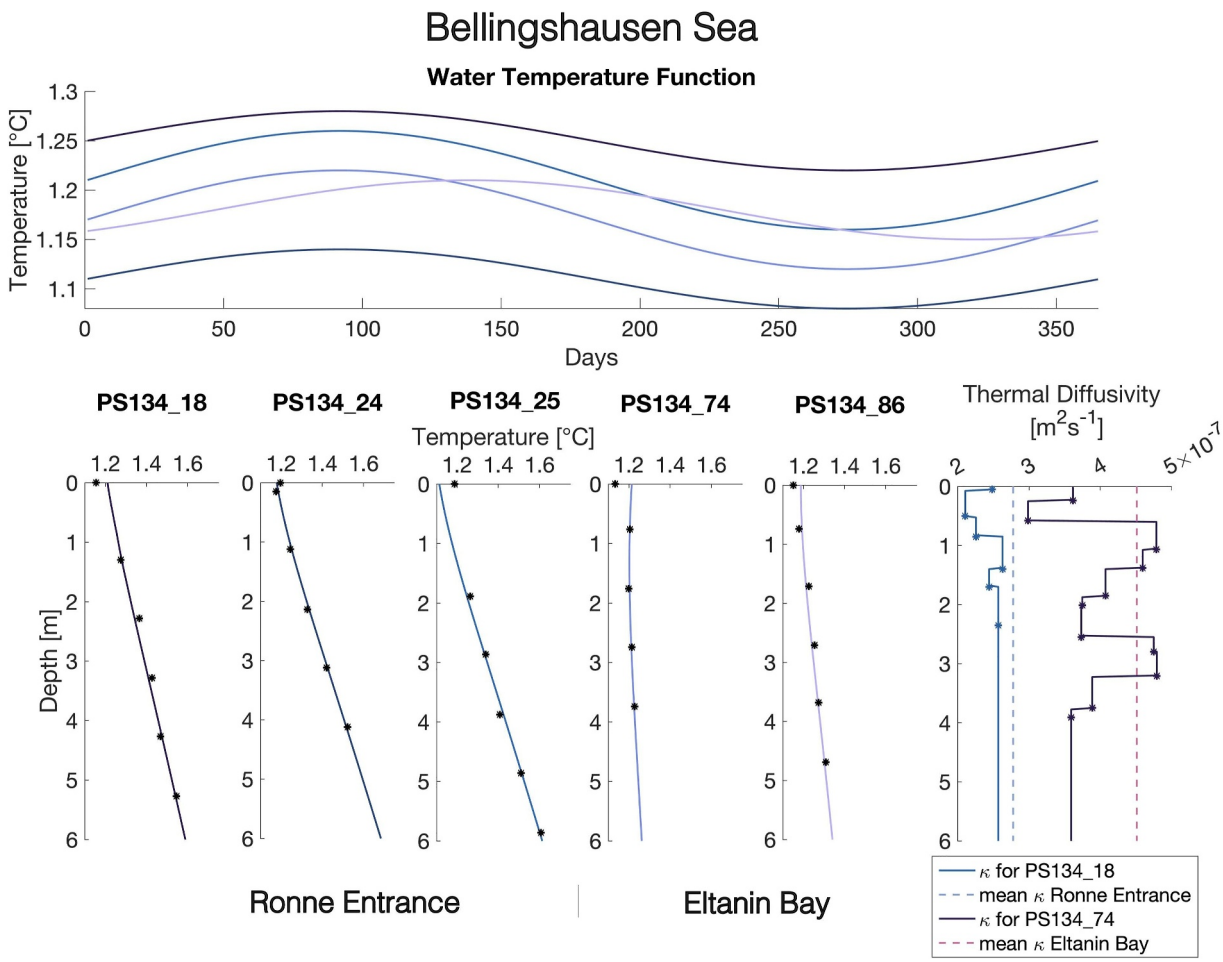


**Figure 7.** The forward model solutions with the lowest relative error for each station. Top: $T_{BWT}(t)$ for each station based on mooring data from the Amundsen Sea. Bottom: Model solution at the day of measurement (blue line) in respect to the measurements from the Bellingshausen Sea (black asterisks) and the used thermal diffusivities (measured (*) and model-interpolated (–)).

### 5.2. Spatial Heterogeneity of the mCDW Temperature

Before investigating the effect of potential mCDW temperature variations, it is necessary to analyze the spatial heterogeneities in the recorded mCDW temperatures. Data sets acquired by seal tags or CTD casts provide some information about the mCDW's pathway, but there are still some gaps in the spatial coverage that need to be addressed (Schubert et al., 2021). The seal tag data recorded an east-west difference across the Bellingshausen Sea of 0.22°C warmer mCDW in the east (Schubert et al., 2021). The analysis of the heat flow sites shows a smaller difference of 0.1°C in the maximum temperature of the mCDW between Ronne Entrance and Eltanin Bay (Figure 6; ∼400–600 m water depth). Further, the stations PS134_74 and PS134_75, closer to the coast in Eltanin Bay (15–20 km, 1.0°C), show a 0.1°C cooler mCDW than records with a 30 km costal distance. This maybe indicative of the cooling and erosion process toward the coast observed earlier at mid-depth temperatures (∼300–500 m, >1.2°C) in the Belgica Trough (Zhang et al., 2016).

The east-west gradient in mCDW temperatures and layer thickness across the Latady Trough and across the Belgica Trough (Schulze Chretien et al., 2021; Zhang et al., 2016) cannot be found for our eastern and western stations in Ronne Entrance or Eltanin Bay, likely due to the observed decrease in the temperature gradient closer to the coast (Schulze Chretien et al., 2021; Zhang et al., 2016). Conversely, the shallower onset of mCDW between 300 and 400 m water depth at the western stations in Eltanin Bay is contrary to this east-west gradient in the mCDW thickness determined by other studies (Schulze Chretien et al., 2021). As multiple and local processes, such as meltwater, deep water formation, or tidal currents, play a role in the vertical water column structure

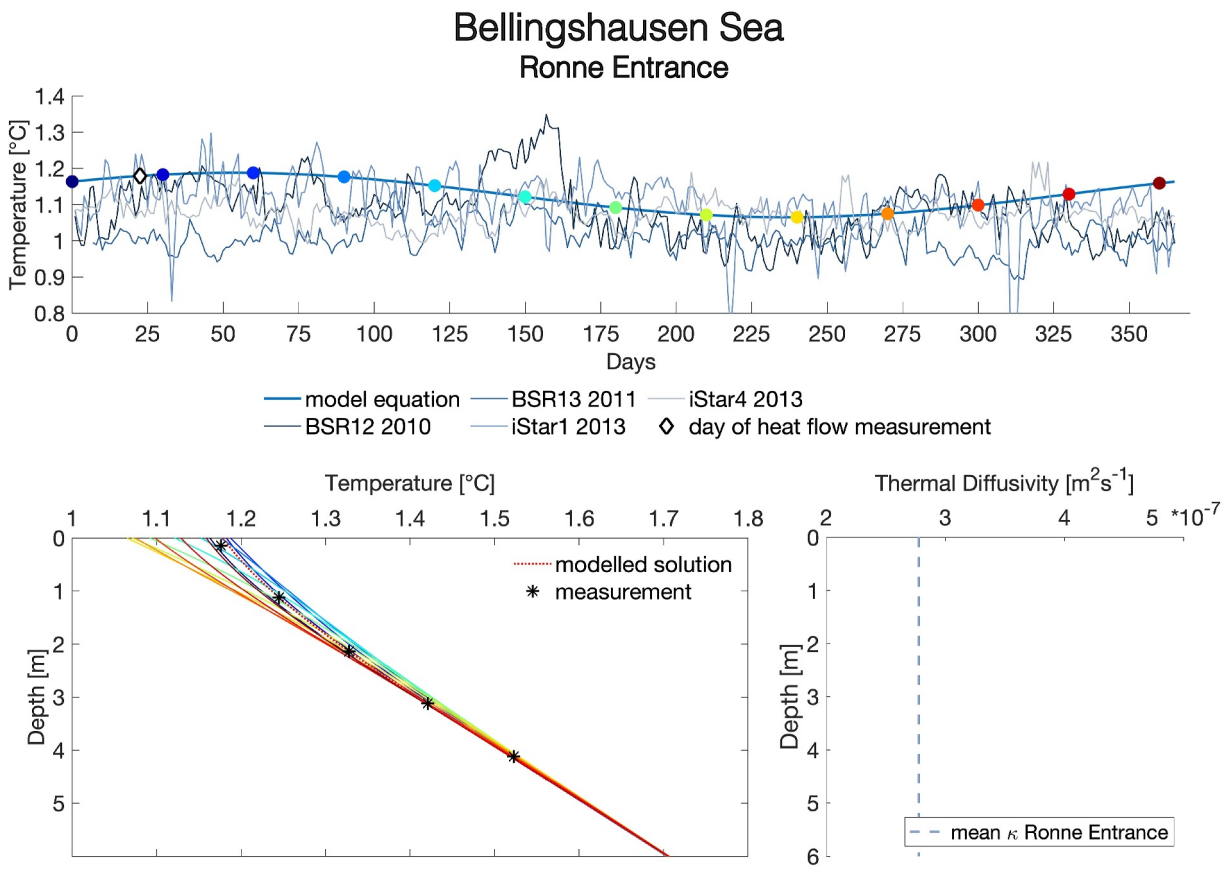


**Figure 8.** Exemplary visualization of inversion result with the lowest model error, station PS134_24, Ronne Entrance, Bellingshausen Sea. Top: The reconstructed $T_{BWT}(t)$ in relation to mooring measurements. Bottom left: Modeled transient geothermal gradients in relation to the sub-bottom temperature measurements. The colors represent a transient geothermal gradient at a certain time of the water temperature time series. Bottom right: Mean thermal diffusivity for Ronne Entrance. Visualization of the inversion results for other stations can be found in Supporting Information S1.

(Schulze Chretien et al., 2021), depth uncertainties in the heat flow lance recordings remain, but the cause of this deviation cannot be explained.

On average, the mCDW temperatures near the seafloor are 0.02°C warmer in Ronne Entrance than in Eltanin Bay, as recorded by our heat flow lance sensors. In Eltanin Bay, the bottom water temperatures decrease slightly with water depth (1.16°C at 829 m to 1.06°C at 1,150 m). In Ronne Entrance, the water depths of the heat flow stations are comparable (680–768 m) and the bottom water temperatures show only minor temperature differences (1.14–1.18°C), with no correlation to their location within Ronne Entrance.

The analysis of the water temperatures recorded with the heat flow lance shows that the mCDW can be detected in the entire study area. The distribution of selected heat flow stations with the largest temperature distortions shows no connection to trends in the mCDW temperature distribution.

### 5.3. Possibility of Seasonal mCDW Temperature Variations

In the Amundsen Sea, the amplitude of the seasonal mCDW temperature cycle varies with water depth. At 500 m, the CDW changes by 1°C, at ~700 m by 0.3°C, and little variations were observed at 900 m water depth (Webber et al., 2017). If the variations observed in the Amundsen Sea are considered comparable to the variations in the Bellingshausen Sea, the inversion results should reconstruct amplitudes of ±0.15°C, as the selected stations in the Bellingshausen Sea are located between 585 and 748 m water depth. With a range of ±0.04–0.08°C, the reconstructed amplitudes for the Bellingshausen Sea remain below comparable amplitudes from the Amundsen Sea (Table 2). However, the forward model with the mooring data as input shows that using an amplitude of

**Table 4**
*The Influence of Annual and Multidecadal Water Temperature Variations on the Heat Flow Determination*

| | | Annual | | | | Multidecadal | |
|---|---|---|---|---|---|---|---|
| | Station | $g$ (°C m$^{-1}$) determined from inversion | $\Delta g$ (°C m$^{-1}$) due to possible $T_{BWT}$ variations | $Q$ (mW m$^{-2}$) determined from inverted $g$ | $\Delta Q$ (mW m$^{-2}$) due to possible $T_{BWT}$ variations | $g$ (°C m$^{-1}$) before 0.3° C/30 yr warming | $Q$ (mW m$^{-2}$) before 0.3° C/30 yr warming |
| Ronne Entrance | PS134_16 | – | – | – | – | 0.101 | 94 |
| | PS134_17 | – | – | – | – | 0.069 | 64 |
| | PS134_18 | 0.059 | ±0.013 (22%) | 48 | ±11 | 0.084 | 69 |
| | PS134_20 | – | – | – | – | 0.071 | 76 |
| | PS134_21 | – | – | – | – | 0.102 | 103 |
| | PS134_24 | 0.097 | ±0.009 (9%) | 90 | ±8 | 0.106 | 98 |
| | PS134_25 | 0.084 | ±0.009 (11%) | 78 | ±8 | 0.105 | 97 |
| | PS134_26 | – | – | – | – | 0.070 | 65 |
| | PS134_27 | – | – | – | – | 0.096 | 89 |
| Eltanin Bay | PS134_70 | – | – | – | – | – | – |
| | PS134_74 | 0.014 | ±0.009 (64%) | 19 | ±12 | 0.034 | 47 |
| | PS134_75 | – | – | – | – | 0.037 | 56 |
| | PS134_76 | – | – | – | – | 0.053 | 80 |
| | PS134_77 | – | – | – | – | 0.042 | 63 |
| | PS134_78 | – | – | – | – | 0.045 | 68 |
| | PS134_79 | – | – | – | – | 0.032 | 48 |
| | PS134_80 | – | – | – | – | – | – |
| | PS134_81 | – | – | – | – | – | – |
| | PS134_82 | – | – | – | – | – | – |
| | PS134_86 | 0.027 | ±0.011 (42%) | 41 | ±17 | 0.043 | 65 |
| | PS134_87 | – | – | – | – | 0.035 | 53 |
| | PS134_88 | – | – | – | – | 0.053 | 80 |

*Note.* Annual variations are represented by the reconstructed geothermal gradients obtained by inverting heat flow station measurements, which have distortions in water and sediment temperatures from a linear trend. Uncertainties $\Delta g$ are based on the transient gradients at minimum and maximum water temperatures over 1 year. Therefore, the heat flow uncertainties represent the possible maximum error when determining the geothermal gradient at different times of the year. Further, calculated geothermal gradients before a 0.3°C/30 years bottom water warming are shown.

±0.15°C increases the model error slightly, nevertheless within the accuracy that can be achieved (Table S4 in Supporting Information S1). Therefore, the possibility of larger amplitude variations in the Bellingshausen Sea cannot be excluded by the model analysis. A correlation between water depth and amplitude of a possible water temperature variation, as observed in the Amundsen Sea, cannot be established as heat flow stations with and without distortions in the geothermal gradient have similar water depths.

For most GHF stations, the best model solution has a phase shift in the water temperature curve with a minimum temperature around the austral summer (October–March). That would be in line with the variability of CDW in the Amundsen Sea, where, besides the northeastern part, lower temperatures have been documented during the austral summer period from November to March (Assmann et al., 2013; Azaneu et al., 2023). In the eastern Bellingshausen Sea, seal tag data confirm that mCDW temperatures are colder in the austral summer than in the winter (Schubert et al., 2021). A more precise evaluation of the phase shifts in the water temperature curve is prevented by interannual mCDW temperature variations (Assmann et al., 2013).

Some studies point out the different positions of the Amundsen and Bellingshausen seas relative to the ASL, which is assumed to cause the mCDW temperature variations. In the Amundsen Sea, the changing position of the ASL leads to changes in wind direction and wind strength over the shelf edge (Thoma et al., 2008). As the Bellingshausen Sea is further east of the ASL, the influence of its changing position is reduced and the isobars fluctuate less in space (Holland et al., 2010).

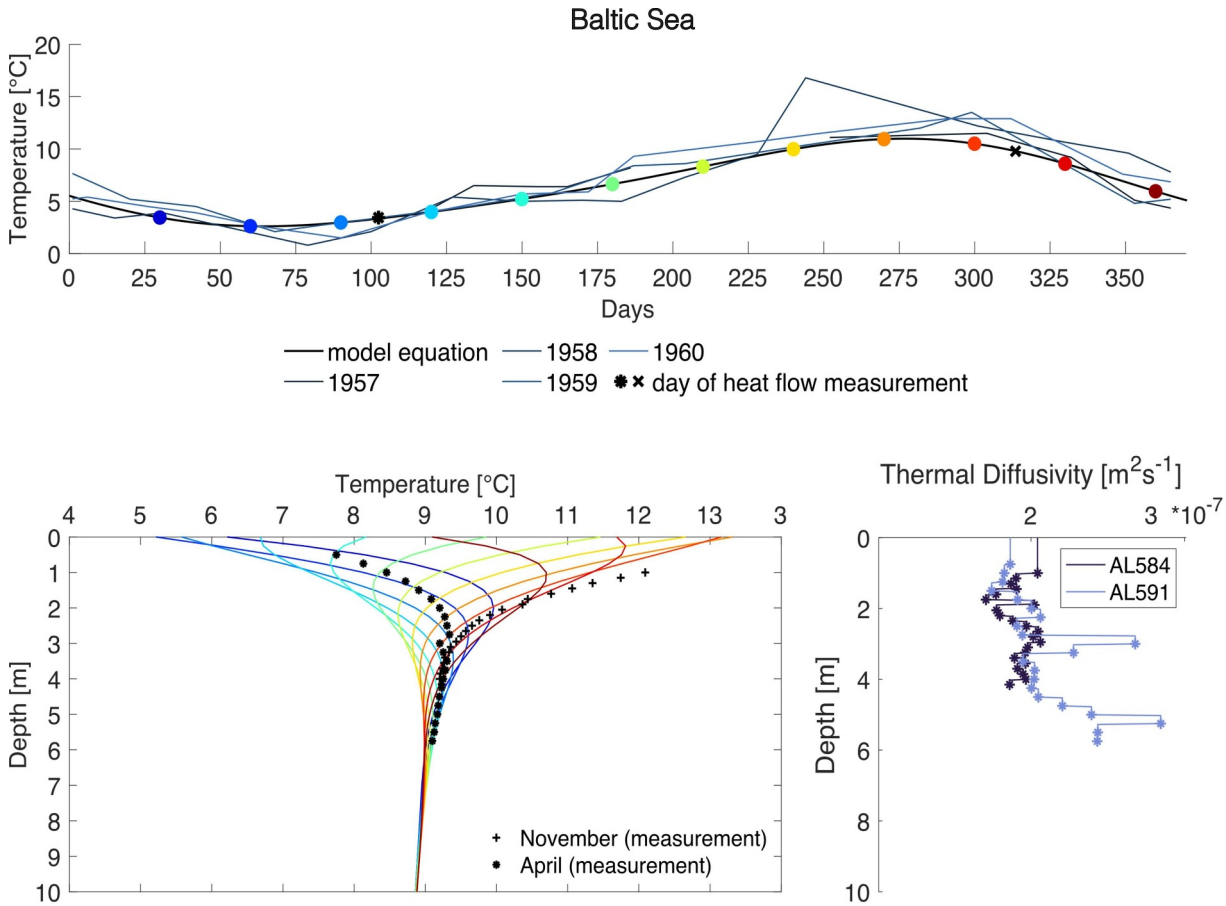


**Figure 9.** Top: $T_{BWT}(t)$ adapted from the forward model with $A = 6.53$°C related to water temperature measurements 1957–1960. Bottom left: Modeled transient geothermal gradients for station VH002/HF002, Baltic Sea, after 66 years in relation to the sub-bottom temperature measurements. Bottom right: The measured (*) and for the model use interpolated (−) thermal diffusivities for station VH002/HF002. This model only considers thermal diffusivities of cruise AL584.

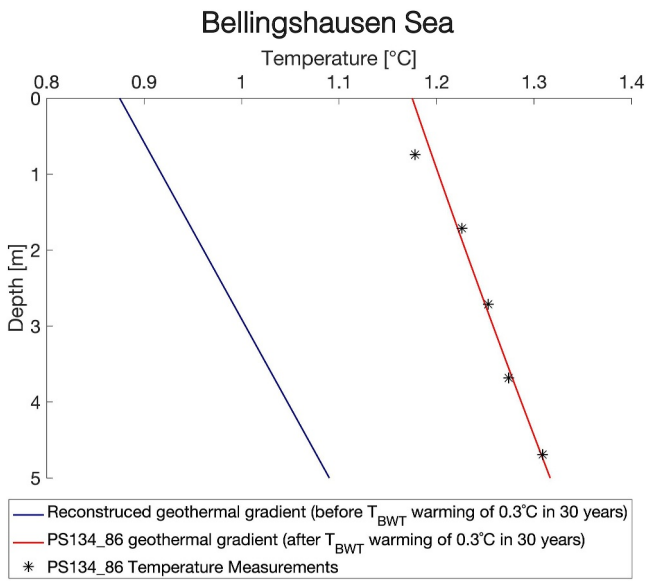


**Figure 10.** Exemplary visualization of the geothermal gradient of station PS134_86, Eltanin Bay, Bellingshausen Sea, derived from measurements (red) and prior to 30 years with constant warming of 0.01°C $yr^{-1}$ (blue).

Nonetheless, the reanalysis by Oelerich et al. (2022) shows a changing water/wind regime and smaller seasonal mCDW changes within the regimes. The amplitudes of these mCDW temperature variations can be of the same order of magnitude as those reconstructed by the inversion; however, they are influenced by interannual variabilities of almost undetectable amplitudes up to ±1°C in 1 year (Oelerich et al., 2022). The variability of deep bottom waters is suggested to be a locally variable process caused by sea ice coverage and air-sea heat fluxes (Oelerich et al., 2022), as highlighted by similar studies from the Amundsen Sea (Webber et al., 2017). Thus, the seasonal mCDW behavior was only found within the coastal polynya (Oelerich et al., 2022), in the same research area where the heat flow measurements were carried out in Eltanin Bay. A recent version of the GLORYS12V1 global ocean physics reanalysis model (E.U. Copernicus Marine Service Information, 2023) shows 1 year prior to the PS134 measurements, bottom water temperature variations with similar amplitudes (±0.10°C, ±0.18°C) in Eltanin Bay as approximated by the water-sediment model, and two temperature minima in austral spring and early austral autumn. In Ronne Entrance, the reanalysis model shows negligible temperature variations (Figure S9 in Supporting Information S1). The local variability of bottom waters would provide a suitable explanation for why distortions in the heat flow measurements are not omnipresent and do not follow certain mCDW pathways or

bathymetric trends, but at the same time can be approximated by seasonal water fluctuations. The inversion results further indicate that the mCDW temperature variations cannot be well represented by a cosine and thus most likely do not exhibit a strong seasonal cycle. Year-round water temperature measurements and long-term monitoring are missing to constrain the pattern of mCDW temperature variability.

### 5.4. Implications for Geothermal Heat Flow Measurements

The water-sediment temperature model indicates that the geothermal gradients in the Bellingshausen Sea are affected by short-term water temperature variations. However, a sensitivity test with the artificially generated data shows that the difference in reconstructed and measured geothermal gradients (2%–10%) falls within the range of estimation inaccuracies due to the inversion (15%, Table S6 in Supporting Information S1). Therefore, it is not possible to differentiate whether the deviations are caused by (seasonal) local water variations or by the uncertainty of the inversion. This shows the model's limitation in resolving precise uncertainties in geothermal gradients caused by short-term water temperature variations for areas with spatial and temporal gaps in the water temperature records. However, the water-sediment model demonstrates a significant theoretical impact of seasonal water variations when determining the transient geothermal gradients at times of minimum and maximum water temperatures (Table 4).

Additionally, the continuous inflow of mCDW adds to the heat flow uncertainties and reduces the heat flow values even further. In the Amundsen Sea, this is expected to contribute to a 20% reduction in the heat flow values (Dziadek et al., 2019). As the Ronne Entrance has slightly warmer water than the Eltanin Bay, it could be assumed that this effect leads to an even greater reduction in the geothermal gradient in the Ronne Entrance. Further, due to the assumed rift extension reaching into Eltanin Bay (Bingham et al., 2012), higher heat flow values could be expected for the western Bellingshausen Sea. However, looking at the trends in heat flow values, the opposite is the case. In general, the heat flow values are ∼27 mW $m^{-2}$ higher in Ronne Entrance than in Eltanin Bay (Table 3). An aspect that could contribute to the different heat flow trends across the Bellingshausen Sea, is its glaciation history. The inner Eltanin Bay deglaciated around 12.3 ka BP, which is 6 ka earlier than the inner Ronne Entrance (Hillenbrand et al., 2010). This could give warm bottom water masses more time to contribute to the reduction of the geothermal gradient in Eltanin Bay. It is difficult to pin down the exact onset of CDW flooding the shelves, but evidence for present CDW in the adjacent Amundsen Sea can be found since at least 10.4 ka BP (Hillenbrand et al., 2017). A longer glaciation of the Ronne Entrance could lead to geothermal gradients showing stronger thermal relics.

Another factor, that plays an important role in the spatial heterogeneity of heat flow, is the bathymetry and the geology. In Ronne Entrance, elevated heat flow values are found in front of the topographic height suggesting a possible connection between the heat flow and topographic, tectonic, or geological processes that affect the thermal parameters. In Eltanin Bay, it must be considered that in areas of highly conductive basement rocks and thick sediment cover, heat is refracted away from the thick sediments and follows the path of higher conductivity (Beardsmore & Cull, 2001). As most of Eltanin Bay has a thin sediment cover over the hard rock, the heat flow lance was deployed in depressions/pockets with at least 5 m of sediment, which could introduce a bias. Thus, the topography and thermal properties of the subsurface may contribute to the low heat flow values measured.

The measured geothermal gradients are also further influenced by the constant ocean warming. Multidecadal and even annual water temperature disturbances are particularly significant for measurements in shallow or medium water depths, for example, in the Baltic Sea or the Bellingshausen Sea shelf, as these are more susceptible to oceanographic and atmospheric temperature events (Bilgili, 2025; Webber et al., 2017).

On the Bellingshausen Sea shelf, ocean warming over 30 years causes significant deviations of the measured geothermal gradients from the steady-state gradient. In the Baltic Sea, constant water warming has impacted the shallow sub-bottom temperatures to a point where a linear temperature increase with depth is no longer observable within the upper meters of the sediment, making a heat flow estimation by lance-based probes impossible. These cases highlight the need to correct marine geothermal gradients measurements for environmental factors and external temperature disturbances to accurately determine heat flow values representative of heat originating from the Earth's interior.

## 6. Conclusions

The influence of annual to multidecadal bottom water temperature variations on the first-ever acquired geothermal measurements from the Bellingshausen Sea was investigated. The forward model based on water temperature records represents the sub-bottom temperature measurements with an acceptable error. However, uncertainties remain with the inversion results due to noisy and interannually variable water temperatures.

The water-sediment model results demonstrate that mCDW variations with colder temperatures in the summer and amplitudes of ±0.03–0.15°C, with tendencies toward lower values, could explain the distortion of the geothermal gradients. However, as distortions in the geothermal gradient are not present at all stations and there is no correlation between the location of the distorted geothermal gradients and the spatial heterogeneity of the mCDW temperature, it is likely that local bottom water variations play a key role.

The geothermal measurements from the Bellingshausen Sea shelf area reveal heat flow values between 47 and 84 mW $m^{-2}$ in Ronne Entrance and between 21 and 57 mW $m^{-2}$ in Eltanin Bay. Annual bottom water temperature variations may account for 2%–10% uncertainty in the determined geothermal gradient. However, higher-resolution records of the mCDW temperature patterns are needed to constrain this uncertainty. The longer-term ocean warming could contribute to a 20%–127% deviation from the true gradient in the Bellingshausen Sea and even lead to a negative geothermal gradient in the Baltic Sea. These results highlight the need to correct marine GHF measurements for external temperature disturbances.

## Data Availability Statement

Temperature and thermal conductivity data of the Baltic Sea project have been handed in to the PANGAEA repository for publication via Dillon and Nehring (2023) and Nehring and Dillion (2024). Thermal conductivities, water, and sediment temperatures of cruise PS134, Bellingshausen Sea, are available from Brand et al. (2025).

**Acknowledgments**

Baltic Sea data were acquired during RV Alkor cruises AL584 and AL591. We would like to thank Regina Usbeck, Franziska Nehring, and Melanie Dillon from FIELAX GmbH for the good cooperation during research cruises AL584 and AL591. We thank Marine Sampling Holland for the provision and operation of their vibrocorer during AL584 and FIELAX for their heat flow probe on AL591. The RV Polarstern expedition PS134 to the Bellingshausen Sea was supported by the AWI under Grant AWI_PS134_02. We thank the master and crew of this vessel for their support. This project was funded by the state of Bremen within the framework of the state program "Promotion of Research, Development and Innovation" (FEI) of the Senator for Economics, Labour and Europe of the Free Hanseatic City of Bremen, and the AWI Research Program "Changing Earth—Sustaining our Future" in Subtopics 2.1 (Warming Climates) and 2.3 (Sea Level Change). This study contributes to the Scientific Research Program "Instabilities and Thresholds in Antarctica" (INSTANT) of the Scientific Committee for Antarctic Research (SCAR). This work was supported by the Deutsche Forschungsgemeinschaft (DFG) in the framework of the priority programme "Antarctic Research with comparative investigations in Arctic ice areas" SPP 1158 by a grant (Grant EB 255/8-1). Open Access funding enabled and organized by Projekt DEAL.

## References

Andujar Marquez, J., Bohórquez, M. A., & Melgar, S. (2016). Ground thermal diffusivity calculation by direct soil temperature measurement. Application to very low enthalpy geothermal energy systems. *Sensors*, *16*(3), 306. https://doi.org/10.3390/s16030306

Assmann, K., Jenkins, A., Shoosmith, D., Walker, D., Jacobs, S., & Nicholls, K. (2013). Variability of circumpolar deep water transport onto the Amundsen Sea continental shelf through a shelf break trough. *Journal of Geophysical Research: Oceans*, *118*(12), 6603–6620. https://doi.org/10.1002/2013JC008871

Azaneu, M., Webber, B., Heywood, K. J., Assmann, K. M., Dotto, T. S., & Abrahamsen, E. P. (2023). Influence of shelf break processes on the transport of warm waters onto the eastern Amundsen Sea Continental Shelf. *Journal of Geophysical Research: Oceans*, *128*(5), e2022JC019535. https://doi.org/10.1029/2022JC019535

Bange, H. W., & Malien, F. (2015). Hydrochemistry from time series station Boknis Eck from 1957 to 2014 [Dataset]. https://doi.org/10.1594/PANGAEA.855693

Beardsmore, G. R., & Cull, J. P. (2001). *Crustal heat flow: A guide to measurement and modelling* (Vol. 334). Cambridge University Press. https://doi.org/10.1017/CBO9780511606021

Bilgili, M. (2025). Trend in global ocean heat content into different depth layers from 1940 to 2050. *Natural Hazards*, *121*(10), 12215–12242. https://doi.org/10.1007/s11069-025-07278-0

Bingham, R. G., Ferraccioli, F., King, E. C., Larter, R. D., Pritchard, H. D., Smith, A. M., & Vaughan, D. G. (2012). Inland thinning of West Antarctic ice sheet steered along subglacial rifts. *Nature*, *487*(7408), 468–471. https://doi.org/10.1038/nature11292

Brakelmann, H., & Stammen, J. (2006). Thermal analysis of submarine cable routes: LSM or FEM? In *Paper presented at the 2006 IEEE International Power and Energy Conference*. https://doi.org/10.1109/PECON.2006.346714

Brand, C., Kaul, N., Lösing, M., & Gohl, K. (2025). Geothermal heat flow data collected during PS134 [Dataset bundled publication]. *PANGAEA*. https://doi.org/10.1594/PANGAEA.984026

Carslaw, H. S., & Jaeger, J. C. (1939). A problem in conduction of heat. *Mathematical Proceedings of the Cambridge Philosophical Society*, *35*(3), 394–404. https://doi.org/10.1017/S0305004100021149

Crameri, F. (2018). Scientific Colour maps. *Zenodo*. https://doi.org/10.5281/ZENODO.1243862

Decagon Devices Inc. (2016). *KD2 Pro thermal properties Analyzer-Operator's manual*. Pullman.

Dillon, M., & Nehring, F. (2023). Thermal conductivity measurements of nearshore sediments in Eckernförde Bay, Baltic Sea aquired during ALKOR cruise AL584 [Dataset]. *Pangaea*. https://doi.org/10.1594/PANGAEA.962163

Dorschel, B., Hehemann, L., Viquerat, S., Warnke, F., Dreutter, S., Schulze Tenberge, Y., et al. (2022). The International bathymetric Chart of the southern ocean version 2 (IBCSO v2) [Dataset]. *PANGAEA*. https://doi.org/10.1594/PANGAEA.937574

Dziadek, R., Gohl, K., & Kaul, N. (2019). Elevated geothermal surface heat flow in the Amundsen Sea Embayment, West Antarctica. *Earth and Planetary Science Letters*, *506*, 530–539. https://doi.org/10.1016/j.epsl.2018.11.003

E.U. Copernicus Marine Service Information (CMEMS). (2023). Global Ocean Physics reanalysis [Dataset]. *Marine Data Store (MDS)*. https://doi.org/10.48670/moi-00021

Fuchs, S., Neumann, F., Norden, B., Beardsmore, G., Chiozzi, P., Colgan, W., et al. (2023). The global heat flow Database: Update 2023. https://doi.org/10.5880/fidgeo.2023.008

GEBCO Compilation Group. (2023). GEBCO 2023 grid [Dataset]. https://doi.org/10.5285/f98b053b-0cbc-6c23-e053-6c86abc0af7b
GEOMAR Helmholtz Centre for Ocean Research Kiel. (2023). BOKNIS ECK. Coastal time series since 30 April 1957 [Dataset]. Retrieved from https://www.bokniseck.de/home
Gohl, K. (2023). The expedition PS134 of the research vessel POLARSTERN to the Bellinghausen sea in 2022/2023. In H. Bornemann & S. Amir Sawadkuhi (Eds.), *Reports on polar and marine research* (Vol. 777). Bremerhaven: Alfred-Wegener-Institut Helmholtz-Zentrum für Polar- und Meeresforschung. https://doi.org/10.57738/BzPM_0777_2023
Haario, H., Laine, M., Mira, A., & Saksman, E. (2006). Dram: Efficient adaptive MCMC. *Statistics and Computing*, *16*(4), 339–354. https://doi.org/10.1007/s11222-006-9438-0
Hartmann, A., & Villinger, H. (2002). Inversion of marine heat flow measurements by expansion of the temperature decay function. *Geophysical Journal International*, *148*(3), 628–636. https://doi.org/10.1046/j.1365-246X.2002.01600.x
Hillenbrand, C.-D., Larter, R. D., Dowdeswell, J., Ehrmann, W., Cofaigh, C. Ó., Benetti, S., et al. (2010). The sedimentary legacy of a palaeo-ice stream on the shelf of the southern Bellingshausen Sea: Clues to West Antarctic glacial history during the Late Quaternary. *Quaternary Science Reviews*, *29*(19–20), 2741–2763. https://doi.org/10.1016/j.quascirev.2010.06.028
Hillenbrand, C.-D., Smith, J. A., Hodell, D. A., Greaves, M., Poole, C. R., Kender, S., et al. (2017). West Antarctic Ice Sheet retreat driven by Holocene warm water incursions. *Nature*, *547*(7661), 43–48. https://doi.org/10.1038/nature22995
Holland, P. R., Jenkins, A., & Holland, D. M. (2010). Ice and ocean processes in the Bellingshausen Sea, Antarctica. *Journal of Geophysical Research*, *115*(C5), D23101. https://doi.org/10.1029/2008JC005219
Huber, B., & Jacobs, S. (2020). Processed temperature, salinity, and current measurement data from the Amundsen Sea acquired during the Nathaniel B. Palmer expedition NBP0901 [Dataset]. *IU.S. Antarctic Program (USAP) Data Center*. https://doi.org/10.1594/IEDA/322014
Irene, E. A. (2005). *Electronic materials science*. Wiley-Interscience.
Jenkins, A., Shoosmith, D., Dutrieux, P., Jacobs, S., Kim, T. W., Lee, S. H., et al. (2018). West Antarctic ice sheet retreat in the Amundsen Sea driven by decadal oceanic variability. *Nature Geoscience*, *11*(10), 733–738. https://doi.org/10.1038/s41561-018-0207-4
Jordan, T. A., Martin, C., Ferraccioli, F., Matsuoka, K., Corr, H., Forsberg, R., et al. (2018). Anomalously high geothermal flux near the South Pole. *Scientific Reports*, *8*(1), 16785. https://doi.org/10.1038/s41598-018-35182-0
Lagarias, J. C., Reeds, J. A., Wright, M. H., & Wright, P. E. (1998). Convergence properties of the Nelder-Mead simplex method in low dimensions. *SIAM Journal on Optimization*, *9*(1), 112–147. https://doi.org/10.1137/S1052623496303470
Laine, M. (2011). DRAM—Delayed rejection adaptive Metropolis [code]. Retrieved from http://helios.fmi.fi/~lainema/dram/
Laine, M. (2018). MCMC toolbox for Matlab [code]. Retrieved from https://mjlaine.github.io/mcmcstat/
Larour, E., Morlighem, M., Seroussi, H., Schiermeier, J., & Rignot, E. (2012). Ice flow sensitivity to geothermal heat flux of Pine Island Glacier, Antarctica. *Journal of Geophysical Research*, *117*(F4), F04023. https://doi.org/10.1029/2012JF002371
Matsuoka, K., Skoglund, A., Roth, G., de Pomereu, J., Griffiths, H., Headland, R., et al. (2021). Quantarctica, an integrated mapping environment for Antarctica, the Southern Ocean, and sub-Antarctic islands. *Environmental Modelling & Software*, *140*, 105015. https://doi.org/10.1016/j.envsoft.2021.105015
Miesner, F. (2018). *Advanced inverse modeling of sediment thermal diffusion processes: Reconstructing temporal variant boundary conditions for the one-dimensional heat equation, (Doctoral Dissertation)*. Universität Bremen. Retrieved from http://nbn-resolving.de/urn:nbn:de:gbv:46-00106636-14
Miesner, F., Lechleiter, A., & Müller, C. (2015). Reconstructing bottom water temperatures from measurements of temperature and thermal diffusivity in marine sediments. *Ocean Science*, *11*(4), 559–571. https://doi.org/10.5194/os-11-559-2015
Müller, C., Usbeck, R., & Miesner, F. (2016). Temperatures in shallow marine sediments: Influence of thermal properties, seasonal forcing, and man-made heat sources. *Applied Thermal Engineering*, *108*, 20–29. https://doi.org/10.1016/j.applthermaleng.2016.07.105
Nehring, F., & Dillon, M. (2024). Thermal conductivity measurements of nearshore sediments in Eckernförde Bay, Baltic Sea aquired during ALKOR cruise AL591 [Dataset]. *Pangaea*. https://doi.org/10.1594/PANGAEA.967368
Neumann, F., Negrete-Aranda, R., Harris, R. N., Contreras, J., Sclater, J. G., & González-Fernández, A. (2017). Systematic heat flow measurements across the Wagner Basin, northern Gulf of California. *Earth and Planetary Science Letters*, *479*, 340–353. https://doi.org/10.1016/j.epsl.2017.09.037
Oelerich, R., Heywood, K. J., Damerell, G. M., & Thompson, A. F. (2022). Wind-induced variability of warm water on the southern Bellingshausen Sea continental shelf. *Journal of Geophysical Research: Oceans*, *127*(11), e2022JC018636. https://doi.org/10.1029/2022JC018636
Pfender, M., & Villinger, H. (2002). Miniaturized data loggers for deep sea sediment temperature gradient measurements. *Marine Geology*, *186*(3), 557–570. https://doi.org/10.1016/S0025-3227(02)00213-X
Ramires, M. L. V., Nieto de Castro, C. A., Nagasaka, Y., Nagashima, A., Assael, M. J., & Wakeham, W. A. (1995). Standard reference data for the thermal conductivity of water. *Journal of Physical and Chemical Reference Data*, *24*(3), 1377–1381. https://doi.org/10.1063/1.555963
Reading, A. M., Stål, T., Halpin, J. A., Lösing, M., Ebbing, J., Shen, W., et al. (2022). Antarctic geothermal heat flow and its implications for tectonics and ice sheets. *Nature Reviews Earth & Environment*, *3*(12), 814–831. https://doi.org/10.1038/s43017-022-00348-y
Schmidtko, S., Heywood, K. J., Thompson, A. F., & Aoki, S. (2014). Multidecadal warming of Antarctic waters. *Science*, *346*(6214), 1227–1231. https://doi.org/10.1126/science.1256117
Schubert, R., Thompson, A. F., Speer, K., Schulze Chretien, L., & Bebieva, Y. (2021). The Antarctic coastal current in the Bellingshausen Sea. *The Cryosphere*, *15*(9), 4179–4199. https://doi.org/10.5194/tc-15-4179-2021
Schulze Chretien, L., Thompson, A., Flexas, M., Speer, K., Swaim, N., Oelerich, R., et al. (2021). The shelf circulation of the Bellingshausen Sea. *Journal of Geophysical Research: Oceans*, *126*(5), e2020JC016871. https://doi.org/10.1029/2020JC016871
Shampine, L. F., & Reichelt, M. W. (1997). The Matlab ode suite. *SIAM Journal on Scientific Computing*, *18*(1), 1–22. https://doi.org/10.1137/S1064827594276424
Skeel, R. D., & Berzins, M. (1990). A method for the spatial discretization of parabolic equations in one space variable. *SIAM Journal on Scientific and Statistical Computing*, *11*(1), 1–32. https://doi.org/10.1137/0911001
Smith, D. A., Hofmann, E. E., Klinck, J. M., & Lascara, C. M. (1999). Hydrography and circulation of the west Antarctic Peninsula continental shelf. *Deep Sea Research Part I: Oceanographic Research Papers*, *46*(6), 925–949. https://doi.org/10.1016/S0967-0637(98)00103-4
Talbot, M. H. (1988). Oceanic environment of George VI ice shelf, Antarctic Peninsula. *Annals of Glaciology*, *11*, 161–164. https://doi.org/10.3189/S0260305500006480
The MathWorks Inc. (2023). *MATLAB function reference*. The MathWork Inc. Retrieved from https://de.mathworks.com/help/pdf_doc/matlab/matlab_ref.pdf
Thoma, M., Jenkins, A., Holland, D., & Jacobs, S. (2008). Modelling circumpolar deep water intrusions on the Amundsen Sea continental shelf, Antarctica. *Geophysical Research Letters*, *35*(18), L18602. https://doi.org/10.1029/2008GL034939
U.K. Natural Environment Research Council. (2018). iSTAR moorings [Dataset]. Retrieved from https://www.bodc.ac.uk

Villinger, H., & Davis, E. E. (1987). A new reduction algorithm for marine heat flow measurements. *Journal of Geophysical Research*, *92*(B12), 12846–12856. https://doi.org/10.1029/JB092iB12p12846

Webber, B. G., Heywood, K. J., Stevens, D. P., Dutrieux, P., Abrahamsen, E. P., Jenkins, A., et al. (2017). Mechanisms driving variability in the ocean forcing of Pine Island Glacier. *Nature Communications*, *8*(1), 14507. https://doi.org/10.1038/ncomms14507

Zhang, X., Thompson, A. F., Flexas, M. M., Roquet, F., & Bornemann, H. (2016). Circulation and meltwater distribution in the Bellingshausen Sea: From shelf break to coast. *Geophysical Research Letters*, *43*(12), 6402–6409. https://doi.org/10.1002/2016GL068998